FULL PAPER

Magnetic Resonance in Medicine 00:00–00 (2014)

Rapid and Accurate T_2 Mapping from Multi–Spin-Echo Data Using Bloch-Simulation-Based Reconstruction

Noam Ben-Eliezer,* Daniel K. Sodickson, and Kai Tobias Block

Purpose: Quantitative T_2-relaxation-based contrast has the potential to provide valuable clinical information. Practical T_2-mapping, however, is impaired either by prohibitively long acquisition times or by contamination of fast multiecho protocols by stimulated and indirect echoes. This work presents a novel postprocessing approach aiming to overcome the common penalties associated with multiecho protocols, and enabling rapid and accurate mapping of T_2 relaxation values.

Methods: Bloch simulations are used to estimate the actual echo-modulation curve (EMC) in a multi–spin-echo experiment. Simulations are repeated for a range of T_2 values and transmit field scales, yielding a database of simulated EMCs, which is then used to identify the T_2 value whose EMC most closely matches the experimentally measured data at each voxel.

Results: T_2 maps of both phantom and in vivo scans were successfully reconstructed, closely matching maps produced from single spin-echo data. Results were consistent over the physiological range of T_2 values and across different experimental settings.

Conclusion: The proposed technique allows accurate T_2 mapping in clinically feasible scan times, free of user- and scanner-dependent variations, while providing a comprehensive framework that can be extended to model other parameters (e.g., T_1, B_1^+, B_0, diffusion) and support arbitrary acquisition schemes. **Magn Reson Med 000:000–000, 2014.**

Key words: quantitative MRI; T_2 mapping

INTRODUCTION

T_2-relaxation-based contrast is one of the most commonly used contrasts for noninvasive diagnosis and characterization of pathologies. Although almost every clinical MRI exam involves acquisition of T_2-weighted images, the interpretation of T_2 contrast still remains visually qualitative, and lacks information on the actual T_2 relaxation values independent of reader, pulse sequence, and imaging device. Quantitative T_2 mapping has demonstrated merit for various applications including neurodegenerative diseases (1,2), characterization of cancerous lesions (3–5), detection of biochemical and biophysical changes in hip and knee cartilage (6–9), diagnosis of stroke (10), assessment of diseased and posttransplant myocardial edema (11,12), and investigation of muscle physiology (13). Nevertheless, genuine quantification of T_2 relaxation values remains challenging in clinical practice, mainly due to the extremely long scan times associated with single spin-echo (SE) acquisitions. These scans extend on the order of tens of minutes, a factor which not only affects patient comfort and throughput but also makes the scans highly vulnerable to motion artifacts. Sensitivity to diffusion presents another important limitation, adding echo time (TE) dependency to the signal decay particularly at long echo times.

Multi-SE pulse sequences [e.g., CPMG (14)] are a commonly used alternative for in vivo T_2 mapping. These sequences sample multiple time points along the T_2 decay for each k-space line during single repetition time, leading to significantly shorter scan times. Moreover, the use of echo spacings that are an order-of-magnitude shorter than the typical TE used in single SE scans results in a significant reduction of diffusion effects in the multiecho sequences (15). These advantages, however, come at the cost of strong signal contamination with stimulated and indirect echoes, generated because each refocusing pulse separates the magnetization into three coherence pathways: the main transverse magnetization inverted by the radiofrequency (RF) pulse, and two spurious pathways representing spins that are stored along the longitudinal axis and spins that are unaffected by the refocusing pulse. A very clear graphical depiction of this process is provided by the phase-graph formalism (16) and other related approaches (17). As illustrated by Hennig (16), a train of spin echoes will generate 3^{ETL} coherence pathways (ETL being the echo train length), whose cumulative contribution will eventually be reflected in the acquired signal. The subset of coherence pathways contributing to each specific echo depends on the refocusing pulse flip-angle and phase, and, furthermore, on the slice profile, which, considering typical use of nonperfect rectangular profiles, intrinsically incorporates a range of flip angles. The resulting T_2 decay of the acquired echo-train will no longer exhibit a pure exponential decay of the form

$$S(t) = S_0 \exp(-t/T_2) \quad [1]$$

but will rather follow a generalized echo-modulation curve (EMC), whose characteristics depend on the relaxation values as well as on a variety of other experimental and physical parameters, for example, T_2, T_1, B_0, B_1^+,

The Bernard and Irene Schwartz Center for Biomedical Imaging, Department of Radiology, New York, University School of Medicine, New York, New York, USA.

Grant sponsor: the National Heath Institute; Grant number: NIH RO1 EB000447.

*Correspondence to: Ben-Eliezer Noam, Ph.D., The Bernard and Irene Schwartz Center for Biomedical Imaging, Department of Radiology, New York, University School of Medicine, New York, NY 10016. E-mail: noam.ben-eliezer@nyumc.org

Additional Supporting Information may be found in the online version of this article.

Correction added after online publication 31 March 2014. An incomplete author list appeared in the original publication and has been corrected to include all coauthors.

Received 17 August 2013; revised 24 December 2013; accepted 10 January 2014

DOI 10.1002/mrm.25156

Published online 00 Month 2014 in Wiley Online Library (wileyonlinelibrary.com).

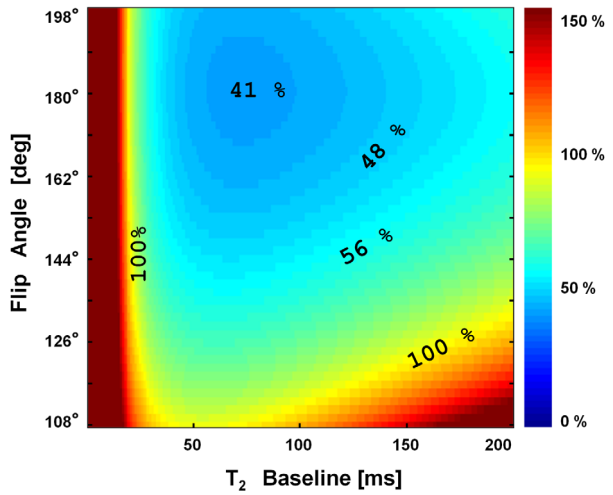

FIG. 1. Simulation of the T_2 bias when fitting a multi-SE decay curve to an exponential model of the form $S(t) = S_0\exp(-t/T_2)$. The bias ranges from 41% to more than a 100% with respect to the underlying baseline value, and reflects the deviation of a multiecho modulation curve from a theoretical exponential decay as a result of stimulated and indirect echoes. The relative error varies primarily as a function of baseline T_2 value and transmit flip angle, with secondary contributions from other experimental parameters delineated in the text. Simulations compared one-dimensional multi- versus single-SE pulse-sequences, assuming perfectly homogeneous B_0 distribution and no diffusion effects. Simulation parameters were TE = [15,30,...,150] ms ($N_{TE} = 10$), $BW_{acq} = 200$ Hz/Px, $\alpha_{Refocusing} = [108°...198°]$, T_1=2 s, slice-thickness ratio of 1.2 between refocusing and excitation RF pulses. Further details are elaborated in the Methods section. [Color figure can be viewed in the online issue, which is available at wileyonlinelibrary.com.]

and diffusion. When fitting a pure exponential curve to the experimental multiecho EMC, erroneous T_2 values will arise, as exemplified in Figure 1, illustrating the percentage error for different T_2 values and for a range of transmit B_1^+ inhomogeneity scales associated either with the natural variation of the flip angles along slice borders, or with inhomogeneity of the B_1^+ field. Two straightforward alternatives for improving the fitting of multi-SE data include excluding either the first, or all odd-numbered echoes from the fit (18). These options, although improving the fitting fidelity, hinder quantification of short T_2 components, make inefficient use of the acquired data, and still result in distorted T_2 values. Other, more sophisticated solutions use analytical or numerical stepwise tracing of all coherence pathways that arise in a multiecho sequence (19–23), incorporate the phase graph formalism into model based-reconstruction approaches (24), or use non SE-based pulse sequence schemes that can be more accurately modeled, yet at the cost of reduced T_2 encoding sensitivity (25,26). Notwithstanding promising preliminary results, many techniques still possess inherent limitations either due to not accounting for relaxation during the RF pulses (20,22–24), flip angle variation along the slice / slab profile (25,26), relying on lengthy three-dimensional (3D) acquisition schemes (20,23), or not allowing straightforward model inversion for deducing a T_2 value from an experimentally measured echo train (19).

In this work, we present a novel approach for the calculation of accurate T_2 maps from multi-SE data. The approach is based on using stepwise Bloch simulations of the experimental pulse sequence to trace all coherence pathways occurring along the echo train and thereby accurately reproduce all resulting stimulated and indirect echoes. These simulations are performed once as a preprocessing step for a range of T_2 values to create a database of echo-modulation curves, each corresponding to a unique T_2 value. The experimentally acquired data are then matched pixel-by-pixel against the database using a best-fit criterion to reveal the samples' true T_2 values. Validations of the proposed technique in comparison to reference single SE measurements are presented in phantoms and in vivo, confirming accuracy and robustness over a range of routinely used clinical settings. Generalizations to multiparametric estimation, for example, joint T_2 and B_1^+ fitting, are exemplified and discussed.

METHODS

Preprocessing: Generation of a Simulated EMC Database

To precisely model the magnetization evolution during multiecho acquisitions, simulations of the prospective pulse sequences were programmed in-house in C++ and MATLAB (The MathWorks Inc., Natick, MA). Simulations were based on time and space propagation of spins according to Bloch equations, and used the hard pulse approximation for simulating the RF pulses (27,28). The exact pulse sequence scheme and the parameter values were obtained through offline simulation of the pulse sequence diagram using Siemens' POET sequence testing tool, providing the amplitudes and timing of each RF and gradient pulse. The exact RF pulse shapes were read from the pulse sequence source code and imported into MATLAB.

Although full volumetric simulations would be ideal for EMC modeling, such simulations are not practical due to their extreme computational intensity and extended runtimes. To facilitate the process, 1D imaging simulations were carried out solely along the slice dimension. This choice can be justified by the fact that the stimulated and indirect echoes are essentially caused by imperfect refocusing pulses encoding solely along the slice dimension and, furthermore, by considering that the flip angle variation along the slice profile can only be accounted for by simulating along the slice dimension. Using this simplifying step, it was possible to use high sampling resolution of *ca* 2000 to 5000 spatial points, offering accurate tracking of all the coherence pathways for spin packets residing at each and every point along the slice profile. The simulated object consisted of a Gaussian spin density distribution (full width at half height = 2.5 cm) positioned at the center of a 4 cm field of view (FOV) and imaged with 4 mm spatial resolution. The simulation's internal resolution was set to 140 μm to account for intrapixel dephasing effects, while the temporal resolution was matched to that used in the actual experiment.

Each run of the simulation generates a single echo-modulation curve, reflecting the intensity of each echo along the train for a given set of parameters. A database of simulated EMCs is created by repeating the simulation for a range of T_2 values ([1...299] ms in steps of 1ms and

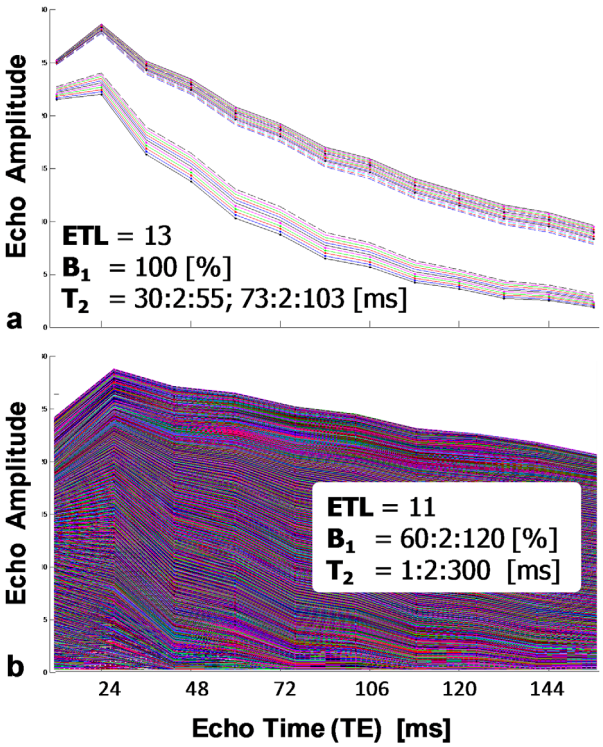

FIG. 2. Examples of a simulated echo-modulation-curve (EMC) database for a multi-SE protocol. **a:** Simplified database containing two ranges of consecutive T_2 values. **b:** Full database, spanning T_2 range of 1 to 300 ms and B_1^+ inhomogeneity scales of 60% to 120%. Both databases were down-sampled to half the actual T_2 and B_1^+ resolutions for visualization purposes. [Color figure can be viewed in the online issue, which is available at wileyonlinelibrary.com.]

[300...1000] in steps of 5 ms) and transmit field (B_1^+) inhomogeneity scales ranging between 60% and 120%, where a value of 100% corresponds to a purely homogeneous B_1^+ field. The calculation time depends on the number of simulated values of the T_2 and B_1^+ parameters and ranged between 1 h for a limited number of a priori known T_2 values to 10 h for full high-resolution simulation of 60 B_1^+ inhomogeneity scales, 450 T_2 values, and ETL = 10. Examples of two databases are illustrated in Figure 2, which shows a simplified set of EMCs corresponding to T_2 = [30...55] and [72...103] ms (Fig. 2a), and a set of T_2 = [1...300] ms and B_1^+ inhomogeneity scales = [60...120] % (Fig. 2b). A pronounced effect of the stimulated echoes can be seen, causing the second echo intensity actually to be higher than the first echo, except for very short T_2 values where the strong signal decay dominates over the stimulated echo effect. The cumulative effect of higher order stimulated echoes is also apparent and manifests as even/odd modulation of the later echoes. Figure 2b hints at a potentially problematic property of the simulated EMC database—namely, that modulation curves corresponding to different [T_2,B_1^+] pairs can sometimes intersect one another. As shown later, this characteristic does not prevent the parameter selection procedure from finding a unique solution during the postprocessing stage. It is, however, expected that the uniqueness will depend on the experimental echo-train length (ETL), where too low ETL values might reduce the robustness of the parameter selection procedure (29). A simplification of the simulation was introduced by fixing the T_1 parameter to a value of 0.5 s for the phantom measurements and 1 s for the in vivo scans. Although T_1 relaxation does take part in the magnetization evolution during an echo train, simulations for a range of T_1 values = [200...4000] ms have shown that for refocusing flip angles in the range [120...180] this parameter has negligible effect on the corresponding EMC, a characteristic which is in agreement with previously reported findings [19,22,23).

MRI Data Acquisition

Experiments were performed on 3 Tesla (T) whole-body MR systems (MAGNETOM Trio / Skyra, Siemens AG Healthcare, Erlangen, Germany) for T_2 phantoms and human subjects. The experimental protocol involved running a product multi-SE sequence, designed to scan each k-space line multiple times following an excitation pulse using a train of equally spaced spin echoes, producing a series of 2D images that correspond to increasing TEs. In addition, a full set of images was acquired with a single SE sequence for a similar range of TEs, providing a more reliable reference for the sample T_2 values. Phantom scans were performed using a 4-channel head coil. The phantom, shown in Figure 3, consisted of a matrix of nine 15 mL test tubes containing purified water doped with $MnCl_2$ concentrations of 0.070, 0.135, 0.270, 0.405, 0.540, 0.675, 0.800, 1.000, 0.540 mM, corresponding to the tubes numbered 1 through 9 (tube #9 was deliberately filled with identical solution to tube #5 to test reproducibility of parameter extraction). This phantom offered a broad range of T_2 test values with T_1/T_2 ratios of 13.8 ± 1.3, similar to human tissues as reported in (18). T_1 values were estimated using Siemens' double-flip-angle T_1 weighted 3D gradient echo protocol. Scans

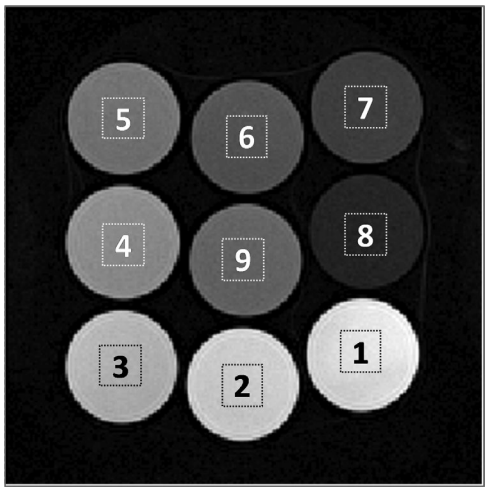

FIG. 3. T_2 weighted fast spin echo image of the nine-tube phantom used in this study. Tubes [1...8] were doped with varying concentrations of manganese chloride ($MnCl_2$) imparting each tube a different T_2 relaxation time. Tubes #9 and #5 were prepared with similar concentrations to verify T_2 mapping consistency over different spatial locations.

were, furthermore, repeated for refocusing angles 180°, 150°, and 120° to assess the stability over a range of commonly used values. Identical experimental parameters were used for the multi- and single SE acquisitions given by [TR = 1500 ms, TE = 12,24,...,216 ms, $N_{TE} = 18$, matrix size = 192 × 192, FOV = 110 × 110 mm^2, slice thickness = 3 mm, refocusing / excitation slice-thickness factor = 1.2, $BW_{acq} = 200$ Hz/Px]. The total scan time was 4:53 min for the multiecho sequence, and 1 h 28 min for the single SE sequence.

In vivo validations were performed by means of brain (N = 5) and prostate (N = 3) scans of healthy volunteers under institutional IRB guidelines and after obtaining written informed consent. Brain scans were performed with a receive-only 12-channel head coil array and used the following parameters: TR = 2500 ms, TE = 15, 30, 45, 60, 75, 90 ms, matrix size = 128 × 102, FOV = 220 × 175 mm^2, slice thickness = 3 mm, $BW_{acq} = 210$ Hz/Px, $\alpha_{refocus} = 180°$, with a total scan time of 2:42 min for the multi-SE (using 2× GRAPPA acceleration), and 26:54 min for the single SE. Prostate scans were performed with a receive-only 6-channel body matrix coil array and used the following parameters: TR = 2500 ms, TE = 15, 30,...,150 ms ($N_{TE} = 10$), matrix size = 128 × 128, FOV = 170 × 170 mm^2, slice thickness = 3 mm, $BW_{acq} = 200$ Hz/Px, $\alpha_{refocus} = 180°$, scan time = 5:20 min for the multi-SE protocol, and TR = 2500 ms, TE = 20, 40, 60, 80, 100 ms, matrix size = 128 × 128, FOV = 170 × 170 mm^2, slice thickness = 3 mm, refocusing / excitation slice-thickness factor = 1.2, $BW_{acq} = 200$ Hz/Px, $\alpha_{refocus} = 180°$, scan time = 26:40 min for the single SE protocol.

Data Postprocessing

T_2 maps were generated from the single SE data by fitting each pixel in the corresponding time-series of DICOM magnitude images to an exponential decay of the form of Eq. [1]. Although the resulting maps may be affected by residual diffusion effects, these are negligible in comparison to the variability of the T_2 values in vivo (30), and the maps were therefore used in this study as a baseline reference for the multi-SE maps. As a second step, T_2 maps were generated from the multi-SE data, first using the same exponential fit used for the single SE data, and then by matching to the precalculated database of simulated EMCs. The EMC matching was done for each pixel by calculating the L2 norm of the difference between the experimental and simulated EMCs, and choosing the EMC giving the minimal value of the L2-norm. This was implemented using a brute force search over the entire database of simulated EMCs, which, due to the limited number of fit parameters, was sufficiently fast for the purpose of this study and was completed in less than 1 min per slice. Following this procedure, a unique pair of $[T_2,B_1^+]$ values was assigned to each pixel, yielding a pair of T_2 and B_1^+ parametric maps of the subject.

Analysis of the EMC Matching Algorithm in the Presence of Noise

Estimation of the EMC matching algorithm's sensitivity to noise was performed through computer simulations by studying the matching process accuracy and precision at different noise levels. To that end, a representative set of echo-modulation curves was extracted from a simulated EMC database and then matched back to the database after adding different levels of noise. The EMC database was constructed for a typical multi-SE parameter set with TE = 12, 24,...,216 ms, $N_{TE} = 18$, slice thickness=3 mm, $BW_{acq} = 200$ Hz/Px. Tested parameter consisted of $T_2 = 20$, 40, 70, 140 ms, $B_1 = 80$, 100, 110 % and SNR levels of 10, 20, 35, 50, 100. The SNR level was defined as the ratio between half of the initial EMC amplitude, and the standard deviation of the synthesized noise vector, modeled to have random Gaussian distribution. To illustrate the SNR definition, Figure 6 shows representative ensembles of EMCs with added noise, while Figure 7 presents simulated images at corresponding SNR levels. The matching process was repeated N = 128 times for each $[B_1,T_2,SNR]$ triplet (each time with a different noise vector), producing an estimate of the accuracy (mean value) and precision (standard deviation) for each parameter set.

RESULTS

$MnCl_2$ Phantom Scans

Table 1 summarizes the measured T_2 values for the nine-tube phantom shown in Figure 3. A clear bias toward higher T_2 values emerges when using an exponential fit to process the multi-SE data, as compared to the reference single SE maps. This effect results mainly from the contribution of stimulated and indirect echoes to later parts of the echo train, causing an artificial elongation of the decay curve. Any deviation from an optimal 180° refocusing flip angle toward lower values amplifies this effect due to higher percentage of the signal being dominated by indirect echoes. A significantly higher accuracy, on the other hand, is achieved across the entire range of T_2 values when using the EMC algorithm. This accuracy was maintained for different refocusing flip angles and was also consistent across two different types of MR scanners. Notwithstanding this improved performance, the EMC algorithm still exhibits increased residual error for lower refocusing flip angles—very similar to the pattern seen for the exponentially fitted values. This bias can presumably be ascribed to the increased effect of T_1 relaxation on the echo train, which is not accounted for in the current implementation. For lower refocusing flip angles, larger fractions of the magnetization are stored along the longitudinal axis where only T_1 relaxation is active. As a final observation, consistency of the EMC algorithm should be noted in accurately estimating the T_2 value of test tubes #5 and #9, containing similar $MnCl_2$ concentrations (0.54 mM) but positioned at different locations within the coil. The B_1^+ profile effect is clearly manifested in this case by the variation of the T_2 errors between the two test tubes when using exponential fitting. The joint $[T_2,B_1^+]$ EMC fit, however, is able to overcome the underlying ΔB_1^+ field inhomogeneity and reproduce consistent T_2 relaxation values for these two test tubes and for all flip angles. Further details regarding the measurement and fitting error of the single-

Table 1
MnCl2 Concentrations and Corresponding T_2 Values for the Phantom Shown in Figure 3 [a]

	MnCl2 [mM]↓		Single-Echo SE [exponential fit]	Multi-Echo SE [exponential fit]			Multi-Echo SE [EMC fit]		
Tube#	α Refocus→	T1 [ms]	180°	180°	150°	120°	180°	150°	120°
[1]	0.070	1424	116.7	158.3	165.9	186.0	115.6	115.4	112.1
[2]	0.135	877	68.5	91.6	94.8	105.1	66.0	65.9	64.7
[3]	0.270	528	36.9	51.7	53.2	62.2	36.3	35.9	35.1
[4]	0.405	363	23.5	34.1	35.5	40.9	23.5	23.4	22.8
[5]	0.540	235	17.9	27.4	28.4	35.3	17.9	17.6	17.2
[6]	0.675	214	14.4	22.5	22.0	27.2	14.2	14.4	14.1
[7]	0.800	155	11.9	19.9	21.7	24.6	11.8	11.8	11.1
[8]	1.000	120	9.7	16.6	17.4	20.6	9.3	8.9	8.4
[9]	0.540	287	17.8	27.1	26.5	32.6	18.0	18.0	17.4
	Average error [%]:			**50.5**	**55.3**	**82.6**	**1.5**	**2.2**	**5.1**

[a] T_2 values were obtained from either single- or multi SE pulse-sequence for three different refocusing flip-angles, and postprocessed using either an exponential fit, or the proposed EMC matching algorithm. Averages of the relative errors for each T_2 value examined are listed in the bottom row. These were calculated as the absolute difference between the single- and multiecho values, divided by the reference single-echo values. Third column holds the T_1 values measured for each test tube, reflecting a relatively constant T_1/T_2 ratio of 13.8 ± 1.3.

and multi-SE acquisition schemes are given in the Discussion.

In Vivo T_2 Mapping

Figure 4 shows representative T_2 mapping of the human brain, comparing maps derived from a single-SE protocol using exponential fitting (Fig. 4a) to ones derived from a multi-SE protocol using exponential fitting (Fig. 4b) and EMC matching (Fig. 4c). As is the case for the phantom results, much better estimation of the T_2 relaxation values is obtained in vivo with the EMC algorithm, and in good agreement with the reference single-SE values. Representative experimental echo-modulation curves are presented

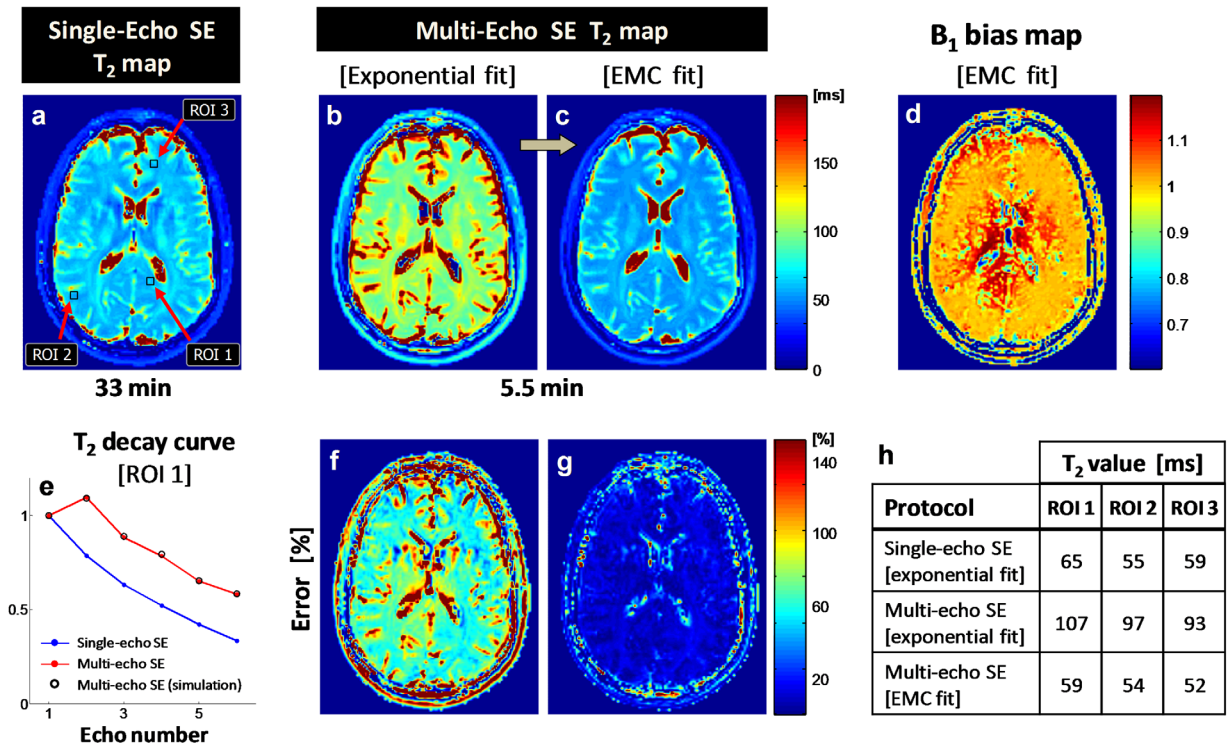

FIG. 4. In vivo T_2 maps of a human brain in a healthy adult volunteer. **a:** T_2 map derived from a single-SE data set and fitted to an exponential decay curve of the form $S(t) = S_0 \exp(-t/T_2)$. **b,c:** T_2 maps derived from a multi-SE data set by means of (b): fitting to the same exponential model as in (a), or (c): matching to the database of simulated EMCs proposed in this report. **d:** B_1^+ bias map, produced by the EMC fitting approach, and resulting from jointly fitting T_2 and B_1^+ values. **e:** Experimental decay curves for ROI #1 marked in panel (a), for single SE (blue) and for multi-SE (red). Empty circles (black) show the simulated EMC that was matched to the experimental multi-echo decay curve. **f,g:** Relative errors for the maps in (b,c), calculated as 100x[(b) – (a)]/(a) and 100x[(c) – (a)]/(a). **h:** Quantitative T_2 values in ROIs 1, 2, and 3, for the maps shown in panels a–c.

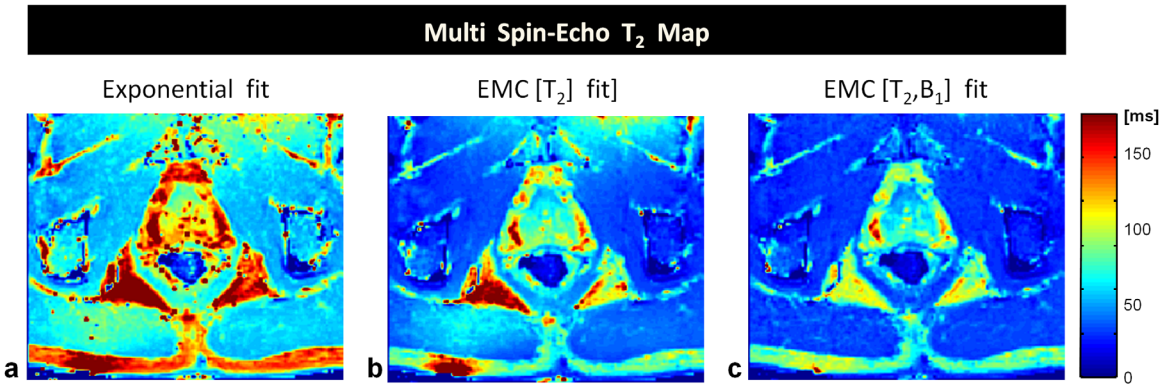

FIG. 5. In vivo T_2 maps of the human prostate in a healthy adult volunteer. Severe motion artifacts, corresponding mainly to involuntary bowel movements, caused strong pixel misalignment during a 32 min acquisition of a single SE data set and prevented reconstruction of a coherent T_2 map. **a:** T_2 maps derived from a multi-SE data set (total acquisition time = 5 min 20 s) and fitted to a standard exponential curve of the form $S(t) = S_0 \exp(-t/T_2)$. Overestimation of the T_2 values is expected in this case due to elongation of the echo-decay curve by stimulated and indirect echoes. **b:** Same data set as in (a) but matched to a database of simulated EMCs, constructed solely for a range of T_2 values. **c:** Same data as in (a) but subjected to a joint $[T_2,B_1^+]$ matching to a database of simulated EMCs, constructed for a range of T_2 and B_1^+ values. The last panel clearly demonstrates the effectiveness of using a joint fit in avoiding transmit-sensitivity-related distortions of the T_2 map. [Color figure can be viewed in the online issue, which is available at wileyonlinelibrary.com.]

in Figure 4e for ROI #1, illustrating the deviation of the multiecho train (red curve) from the pure exponential decay of the single SE train (blue curve), and showing the simulated EMC that was assigned to this voxel (empty black circles). The accuracy provided by the EMC algorithm can be also appreciated from the quantitative comparisons in Figure 4h, and from the full field-of-view difference maps in Figure 4f,g, calculated by dividing the absolute difference between the single- and multi-SE maps by the reference single-echo value. The residual errors seen in Figure 4g might be attributed to inaccuracies of the EMC algorithm. However, they might also reflect true physical inconsistencies between the single- and multiecho acquisitions, or artifacts in the lengthy (33 min) single-echo acquisitions themselves. These effects include slice misregistration and CSF pulsation artifacts, which appear to prevent reliable fitting in some regions of the single SE T_2 map. In addition to the T_2 relaxation map, the EMC fitting process also generated a B_1^+ bias map, shown in Figure 4d. As mentioned above, jointly fitting T_2 and B_1^+ improves the T_2-map accuracy by accounting for any inhomogeneities in the B_1^+ field. In practice, however, Figure 4d constitutes rather a general bias map, which, although heavily weighted by the B_1^+ inhomogeneity profile, embodies the effect of any experimental parameter that was kept invariant during the EMC database calculation. Additional interpretation of this map is given in the Discussion section.

Figure 5 shows representative T_2 maps from a prostate scan. In this application, generation of a reference single SE map was infeasible due to significant prostrate motion caused by involuntary bowel activity during the long acquisition time. The faster multi-SE protocol was able to collect data with reduced motion artifacts and allowed calculation of the T_2 maps shown in Figure 5c–e. Apart from the EMC algorithm's basic capability for unraveling what we believe are the true tissue T_2 values, this example underscores the importance of using a joint $[T_2,B_1^+]$ fit in situations where the coil transmit sensitivities vary significantly within the FOV. Juxtaposing the map in Figure 5c, where only T_2 was fitted, with the one in Figure 5d reveals the efficiency of the EMC algorithm in removing this bias and reinstating a more homogeneous T_2 relaxation map.

Accuracy and Precision of the EMC Algorithm in the Presence of Noise

Summary of the noise / error propagation analysis is presented in Figures 6 and 7. Significantly higher accuracy is obtained when using the EMC algorithm as compared to conventional exponential fit, once again reflecting the strong bias incurred when fitting multi-SE data to the theoretical model in Eq. [1]. The EMC algorithm, furthermore, provides higher precision, manifested by the lower standard-deviation obtained with this approach. Full numerical results are summarized in the online Supporting Information. The error in the EMC fitted T_2 values increases at high noise levels with a mean error of 0.4, 1.0, 1.5, 2.8, and 5.4 % for SNR = 10, 20, 35, 50, and 100, respectively. These errors, however, are still lower than the corresponding values for the exponential fit, namely 58.0, 58.9, 60.5, 65.8, and 79.9 %. A similar trend was seen in the fitting precision at low SNR given by a standard deviation of 0.4, 0.8, 1.1, 2.0, and 3.7 ms for the EMC algorithm versus 1.2, 2.4, 3.3, 5.6, and 10.5 ms for exponential fitting.

DISCUSSION

Quantitative in vivo mapping of T_2 relaxation has been a long standing challenge. As of today, only single SE sequences provide stable, and relatively reliable, T_2 values in vivo. Although pure 3D multi-SE protocols provide an alternative T_2 mapping approach, the choice of multislice single-SE as a reference technique in this study was motivated by the extensive scan time associated with 3D acquisitions, making these more motion sensitive and hence less suitable for in vivo validations.

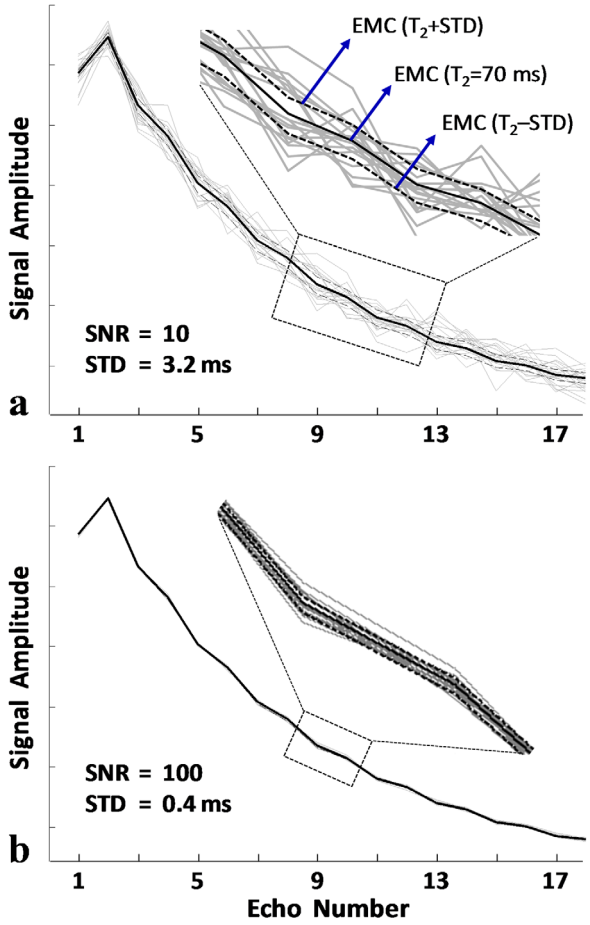

FIG. 6. Illustration of the noise analysis procedure for $B_1 = 100$ %, $T_2 = 70$ ms, at SNR levels of 10 (**a**) and 100 (**b**). Estimation of the EMC matching algorithm's sensitivity to noise was performed through computer simulations by studying the matching process accuracy and precision at different noise levels. To that end, a representative echo-modulation curve (black solid line) was extracted from a simulated EMC database and then matched back to the database after adding noise at different SNR levels. The process was repeated N = 128 times (gray solid lines), producing an estimate of the accuracy (mean value) and precision (standard deviation) for each [B_1,T_2,SNR] parameter set. Black dashed lines in the Figure represent EMCs at T_2 values located one standard-deviation above and below the representative echo-modulation curve, graphically illustrating the standard deviation of the matching process under the given noise level. [Color figure can be viewed in the online issue, which is available at wileyonlinelibrary.com.]

Multislice multiecho sequence schemes offer significant decrease in scan time, yet are affected by strong contamination from stimulated and indirect echoes, leading to nonexponential T_2 decay that depends on a mixture of experimental factors such as pulse sequence timing, magnetic field inhomogeneities, flip angle variation along the excitation / refocusing slice profiles, type of crusher gradients, and more. Thus, to achieve sufficient accuracy and independence from the experimental setup, it is necessary to account for these parameters. The EMC algorithm presented in this work addresses this complexity by using comprehensive Bloch simulations, which not only model the abovementioned factors but can be generalized to incorporate other experimental parameter or acquisition schemes. The ensuing T_2 maps show high correlation to maps acquired using classic SE scans and, more importantly, offer invariance to the chosen sequence parameter values and acquisition schemes. This stability becomes very useful and indeed critical for conducting cross-platform or multicenter studies where the use of different scanner hardware, software versions, or parameter sets can lead to spurious variability of T_2 values.

The bias map shown in Figure 4d complements the T_2-map information produced by the EMC algorithm and reflects the correction achieved using a joint [T_2,B_1^+] fitting procedure. Although this map originates from fitting over a range of B_1^+ inhomogeneity scales (and as such is strongly influenced by the flip angle profile) it cannot be considered a true B_1^+ map as it also embodies second order distortions caused by B_0 inhomogeneities, T_1 relaxation and diffusion. Previous reports as well as our own simulations have shown these to have minor effects on the experimental EMC shape for the T_2-mapping conditions used in this study, hence justifying their exclusion as separate parameters from the fitting process. This being said, alternative pulse sequence designs can actually be used to accentuate these effects and therefore to encode them, for example, by using low refocusing flip angles and short TRs to encode T_1, or gradient pulses to encode diffusion. Extending the simulated EMC database to accommodate additional parameters would then result in separation of the bias map into its underlying components, and would allow retrospective reconstruction of multiple contrasts from a single acquisition (contrary to the classical approach where each contrast is acquired during a separate scan). Further generalizations are also possible and involve, for example, modeling of the proton density, or fitting multiple T_2 components by extending the EMC matching process from a single T_2 to a multi-T_2 fitting of the form

$$EMC^{\text{experimental}} = \sum_i a_i \cdot \left(EMC^{simulated}_{T_2^i} \right) \quad s.t. \sum a_i = 1 \qquad [2]$$

Although theoretically straightforward, extending the matching procedure in this way will lead to a significant increase in the computation time due to the larger search space. This poses a challenge when using standard desktop PCs and might require replacing the simple brute-force search procedure used in this proof-of-principle study by a more sophisticated optimization approach.

Such extensions would be in line with a general trend toward simultaneous mapping of multiple parameters. Several multiparametric techniques have recently been published, where analytically or numerically calculated signal-models are matched to data that is acquired using customized pulse sequence schemes (25,26,31,32). The individual approaches differ mainly in the signal model they assume and in the manner by which the parameters are encoded into the acquisition. Some techniques formulate the multiparametric estimation as inverse problem and include an analytical signal model into the forward operation (33,34). Other techniques use highly

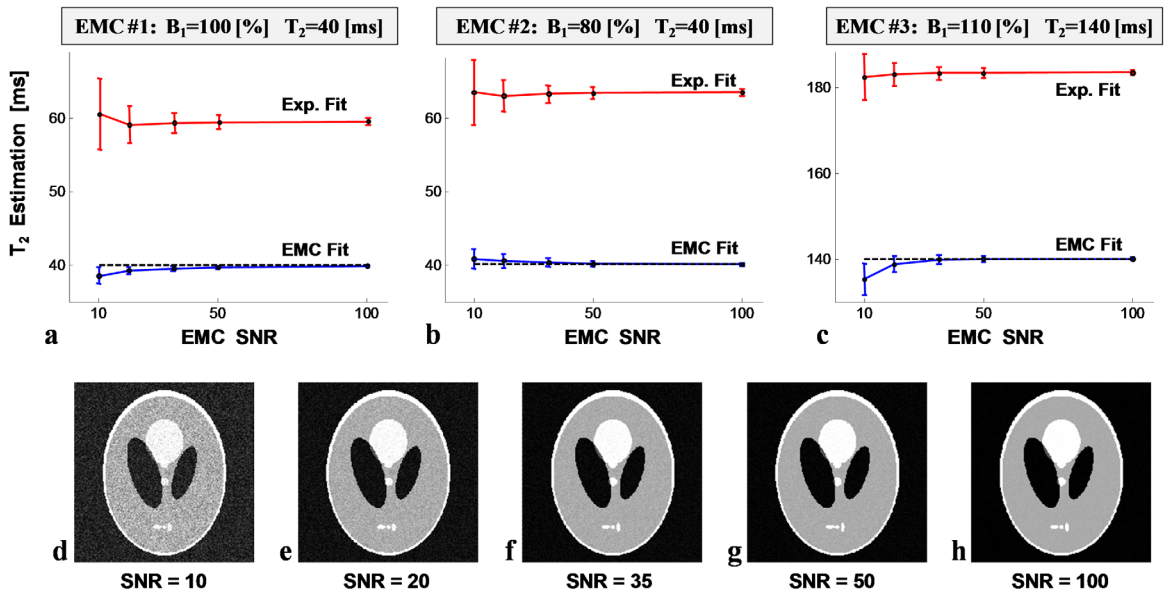

FIG. 7. EMC matching algorithm's performance in the presence of noise. **a–c:** Accuracy (mean value) and precision (one standard-deviation error bars) of T_2 values, estimated using the EMC matching algorithm (blue) and conventional exponential fitting (red), as a function of EMC SNR for three representative $[B_1,T_2]$ value pairs. Black dashed line shows the true underlying T_2 value for each representative echo-modulation curve. **d–h:** Images of a synthesized Shepp-Logan phantom at SNR levels corresponding to those shown in panels a–c. [Color figure can be viewed in the online issue, which is available at wileyonlinelibrary.com.]

incoherent undersampling to shorten the acquisition times, for example, the pioneering works by Doneva et al (35) and the Magnetic Resonance Fingerprinting approach (36), which relies on the incoherency of the undersampling patterns and applies a pattern-recognition algorithm to extract the underlying MR parameters. While the EMC approach was not originally designed to handle incoherent sampling patterns and focused on obtaining high accuracy with clinically established multiecho pulse sequences, use of incoherent sampling schemes can nonetheless still be realized, yet would require incorporation of additional model-based or compressed-sensing techniques to reconstruct fully sampled data before applying the EMC fitting procedure. Rigorous comparison of the EMC algorithm with existing multiparametric techniques and other T_2 mapping approaches such as the slice-resolved EPG method was not performed in this study and will be pursued in future work.

Evaluation of the accuracy of EMC-based parameter selection was done in this study by comparing the results to single SE based T_2 maps. Although a quantitative fitting error can be estimated for these single SE reference maps through a mathematical goodness-of-fit criterion, the same cannot be applied for the EMC parameter selection procedure as it is not based on a simple analytic model. A closed-form expression for the fitting error in the EMC-based T_2 maps is, therefore, not available and other approaches to estimate this value are currently being pursed. Numerical assessment of noise propagation in the EMC algorithm (using a Monte-Carlo approach) and analysis of its sensitivity to small changes in the echo-modulation curves is presented in Figure 7, which illustrates the method's robustness down to SNR levels around 10 and to its superiority over conventional exponential fitting for any SNR level. Due to the use of magnitude images in the fitting process we expect Rician noise distributions to characterize the later echoes where the T_2 decay is strongest (37). This, however, would affect the single-SE and multi-SE data similarly regardless of the fitting technique used, and should therefore not bias the comparison between the corresponding T_2 maps. In practice, the T_2 maps reconstructed using the EMC algorithm exhibit high accuracy with respect to the reference values and, more importantly, address the challenge illustrated in Figure 1—namely that the measurement bias is dependent on the underlying T_2 baseline value. It is important to note, however, that even the corrected T_2 values still do not represent the physical spin–spin relaxation times of the tissue and are rather a spatiotemporal average over multiple mesoscopic domains residing within each macroscopic voxel. This, in turn, relates to another important factor contributing to the signal decay, namely diffusion. At short time scales, this decay will be governed simply by the tissue diffusion coefficient. When longer echo-spacing is used, spins will start to "sample" their surroundings and even traverse different T_2 domains, causing the diffusion-related decay to correlate with the mesoscopic length scale within the tissue (38). Although this effect is expected to be more pronounced in single SE protocols (due to the long echo-spacing used in this type of sequence), subpixel information might still be deduced from accurate multiecho measurement of the macroscopic T_2 with regard to the mesoscopic length scale, for example, by means of fitting for multiple T_2 compartments, or by comparing data sets acquired using different echo-spacing durations.

The high reliability and stability of T_2 mapping achieved with the EMC algorithm can provide a starting point for improving the investigation of diseases in areas where fast and accurate quantitative assessment of the

T_2 relaxation time is essential but impractical in clinical routine. Common examples are neurodegenerative diseases that are associated with demyelination. In this case, potential biomarkers such as myelin-water fraction and extra/intracellular water fraction are calculated based on numeric classification of the tissue T_2. As recently reported (39), existing techniques for estimating these parameters exhibit significant variability, which can be attributed to differences between their underlying models or to the simplifying assumptions incorporated in each technique. By closely matching the EMC-database simulations to the actual acquisition protocol, the presented technique offers faithful reconstruction of the object's T_2 relaxation values, which might help standardize quantitative T_2 assessment for clinical applications.

ACKNOWLEDGMENTS

The authors thank Dr. Ricardo Otazo for fruitful discussions. Noam Ben-Eliezer thanks the Helen and Martin Kimmel foundation for financial support.

REFERENCES

1. Ceccarelli A, Rocca M, Neema M, Martinelli V, Arora A, Tauhid S, Ghezzi A, Comi G, Bakshi R, Filippi M. Deep gray matter T2 hypointensity is present in patients with clinically isolated syndromes suggestive of multiple sclerosis. Mult Scler 2010;16:39–44.
2. Lund H, Jonsson A, Andersen J, Rostrup E, Paulson O, Sorensen P. Cognitive deficits in multiple sclerosis: correlations with T2 changes in normal appearing brain tissue. Acta Neurol Scand 2012;125:338–344.
3. Roebuck J, Haker S, Mitsouras D, Rybicki F, Tempany C, Mulkern R. Carr-Purcell-Meiboom-Gill imaging of prostate cancer: quantitative T2 values for cancer discrimination. Magn Reson Imaging 2009;27:497–502.
4. Liu W, Turkbey B, Senegas J, Remmele S, Xu S, Kruecker J, Bernardo M, Wood B, Pinto P, Choyke P. Accelerated T2 mapping for characterization of prostate cancer. Magn Reson Med 2011;65:1400–1406.
5. Farraher S, Jara H, Chang K, Ozonoff A, Soto JA. Differentiation of hepatocellular carcinoma and hepatic metastasis from cysts and hemangiomas with calculated T2 relaxation times and the T1/T2 relaxation times ratio. J Magn Reson Imaging 2006;24:1333–1341.
6. Mosher T, Dardzinski B. Cartilage MRI T2 relaxation time mapping: overview and applications. Semin Musculoskelet Radiol 2004;8:355–368.
7. Pan J, Pialat J, Joseph T, Kuo D, Joseph G, Nevitt M, Link T. Knee cartilage T2 characteristics and evolution in relation to morphologic abnormalities detected at 3-T MR imaging: a longitudinal study of the normal control cohort from the Osteoarthritis Initiative. Radiology 2011;261:507–515.
8. Nishii T, Shiomi T, Tanaka H, Yamazaki Y, Murase K, Sugano N. Loaded cartilage T2 mapping in patients with hip dysplasia. Radiology 2010;256:955–965.
9. Son M, Goodman S, Hargreaves B, Gold G, Levenston M. Regional variation in T1? and T2 times in osteoarthritic human menisci: correlation with mechanical properties and matrix composition. Osteoarthritis Cartilage 2013;21:796–805.
10. Siemonsen S, Mouridsen K, Holst B, Ries T, Finsterbusch J, Thomalla G, Ostergaard L, Fiehler J. Quantitative t2 values predict time from symptom onset in acute stroke patients. Stroke 2009;40:1612–1616.
11. Giri S, Chung Y, Merchant A, Mihai G, Rajagopalan S, Raman S, Simonetti O. T2 quantification for improved detection of myocardial edema. J Cardiovasc Magn Reson 2009;11:56.
12. Usman A, Taimen K, Wasielewski M, et al. Cardiac magnetic resonance T2 mapping in the monitoring and follow-up of acute cardiac transplant rejection: a pilot study. Circ Cardiovasc Imaging 2012;5:782–790.
13. Patten C, Meyer R, Fleckenstein J. T2 mapping of muscle. Semin Musculoskelet Radiol 2003;7:297–305.
14. Meiboom S, Gill D. Modified spin-echo method for measuring nuclear relaxation times. Rev Sci Instrum 1958;29:688–691.
15. Carr H, Purcell E. Effects of diffusion on free precession in nuclear magnetic resonance experiments. Phys Rev 1954;94:630–638.
16. Hennig J. Multiecho imaging sequences with low refocusing flip angles. J Magn Reson 1988;78:397–407.
17. Sodickson A, Cory D. A generalized k-space formalism for treating the spatial aspects of a variety of NMR experiments. Prog Nucl Magn Reson Spectrosc 1998;33:77–108.
18. Kim D, Jensen J, Wu E, Sheth S, Brittenham G. Breathhold multiecho fast spin-echo pulse sequence for accurate R2 measurement in the heart and liver. Magn Reson Med 2009;62:300–306.
19. Zur Y. An algorithm to calculate the NMR signal of a multi spin-echo sequence with relaxation and spin-diffusion. J Magn Reson 2004;171:97–106.
20. Lukzen N, Petrova M, Koptyug I, Savelov A, Sagdeev R. The generating functions formalism for the analysis of spin response to the periodic trains of RF pulses. Echo sequences with arbitrary refocusing angles and resonance offsets. J Magn Reson 2009;196:164–169.
21. Petrovic A, Scheurer E, Yen K, Stollberger R. Improved T2-quantification with slice selective MSE-sequences. In Proceedings of the 19th Annual Meeting of ISMRM, Montreal, Canada, 2011. Abstract 2749.
22. Lebel R, Wilman A. Transverse relaxometry with stimulated echo compensation. Magn Reson Med 2010;64:1005–1014.
23. Prasloski T, Madler B, Xiang Q, MacKay A, Jones C. Applications of stimulated echo correction to multicomponent T2 analysis. Magn Reson Med 2012;67:1803–1814.
24. Huang C, Bilgin A, Barr T, Altbach M. T2 relaxometry with indirect echo compensation from highly undersampled data. Magn Reson Med 2012;70:1026–1037.
25. Deoni S, Rutt B, Peters T. Rapid combined T1 and T2 mapping using gradient recalled acquisition in the steady state. Magn Reson Med 2003;49:515–526.
26. Schmitt P, Griswold M, Jakob P, Kotas M, Gulani V, Flentje M, Haase A. Inversion recovery TrueFISP: quantification of T(1), T(2), and spin density. Magn Reson Med 2004;51:661–667.
27. Subramanian VH, Eleff SM, Rehn S, Leigh JS. An exact synthesis procedure for frequency selective pulses. In Proceedings of the 4th Annual Meeting of Society for Magnetic Resonance in Medicine, Boston, Massachusetts, USA, 1985. p. 1452–1453.
28. Pauly JM, LeRoux P, Nishimura DG, Macovski A. Parameter relations for the Shinnar–LeRoux selective excitation pulse design algorithm. IEEE Trans Med Imaging 1991;10:53–65.
29. Uddin MN, Marc Lebel R, Wilman AH. Transverse relaxometry with reduced echo train lengths via stimulated echo compensation. Magn Reson Med 2013;70:1340–1346.
30. Stanisz G, Odrobina E, Pun J, Escaravage M, Graham S, Bronskill M, Henkelman RM. T1, T2 Relaxation and magnetization transfer in tissue at 3T. Magn Reson Med 2005;54:507–512.
31. Warntjes J, Dahlqvist O, Lundberg P. Novel method for rapid, simultaneous T1, T*2, and proton density quantification. Magn Reson Med 2007;57:528–537.
32. Ehses P, Seiberlich N, Ma D, Breuer F, Jakob P, Griswold M, Gulani V. IR TrueFISP with a golden-ratio-based radial readout: fast quantification of T1, T2, and proton density. Magn Reson Med 2013;69:71–81.
33. Block K, Uecker M, Frahm J. Model-based iterative reconstruction for radial fast spin-echo MRI. IEEE Trans Med Imaging 2009;28:1759–1769.
34. Sumpf T, Uecker M, Boretius S, Frahm J. Model-based nonlinear inverse reconstruction for T2 mapping using highly undersampled spin-echo MRI. J Magn Reson Imaging 2011;34:420–428.
35. Doneva M, Bornert P, Eggers H, Stehning C, Senegas J, Mertins A. Compressed sensing reconstruction for magnetic resonance parameter mapping. Magn Reson Med 2010;64:1114–1120.
36. Ma D, Gulani V, Seiberlich N, Liu K, Sunshine J, Duerk J, Griswold M. Magnetic resonance fingerprinting. Nature 2013;14:187–192.
37. Gudbjartsson H, Patz S. The Rician distribution of noisy MRI data. Magn Reson Med 1995;34:910–914.
38. Novikov D, Kiselev V. Transverse NMR relaxation in magnetically heterogeneous media. J Magn Reson 2008;195:33–39.
39. Zhang J, Kolind SH, MacKay AL. Comparison of myelin water fraction brain images using multi-echo T2-weighted GRASE relaxation and steady-state methods. In Proceedings of the 21st Annual Meeting of ISMRM, Salt Lake City, Utah, USA, 2013. Abstract 1103.